Available online at www.sciencedirect.com
ScienceDirect
International Journal of Heat and Mass Transfer 51 (2008) 2950–2966
International Journal of HEAT and MASS TRANSFER
www.elsevier.com/locate/ijhmt

Investigation of dimpled fins for heat transfer enhancement in compact heat exchangers

Mohammad A. Elyyan, Ali Rozati, Danesh K. Tafti *

High Performance Computational Fluids-Thermal Sciences and Engineering Laboratory, Mechanical Engineering Department, Virginia Polytechnic Institute and State University, Blacksburg, VA 24061, USA

Received 23 March 2007; received in revised form 10 September 2007
Available online 5 November 2007

Abstract

Direct and Large-Eddy simulations are conducted in a fin bank with dimples and protrusions over a Reynolds number range of $Re_H = 200$ to 15,000, encompassing laminar, transitional and fully turbulent regimes. Two dimple-protrusion geometries are studied in which the same imprint pattern is investigated for two different channel heights or fin pitches, Case 1 with twice the fin pitch of Case 2. The smaller fin pitch configuration (Case 2) develops flow instabilities at $Re_H = 450$, whereas Case 1 undergoes transition at $Re_H = 900$. Case 2, exhibits higher Nusselt numbers and friction coefficients in the low Reynolds number regime before Case 1 transitions to turbulence, after which, the differences between the two decreases considerably in the fully turbulent regime. Vorticity generated within the dimple cavity and at the dimple rim contribute substantially to heat transfer augmentation on the dimple side, whereas flow impingement and acceleration between protrusions contribute substantially on the protrusion side. While friction drag dominates losses in Case 1 at low Reynolds numbers, both form and friction drag contributed equally in Case 2. As the Reynolds number increases to fully turbulent flow, form drag dominates in both cases, contributing about 80% to the total losses. While both geometries are viable and competitive with other augmentation surfaces in the turbulent regime, Case 2 with larger feature sizes with respect to the fin pitch is more appropriate in the low Reynolds number regime $Re_H < 2000$, which makes up most of the operating range of typical compact heat exchangers.

Keywords: Dimples; Compact heat exchangers; LES

1. Introduction

The science and engineering of air-side heat transfer enhancement plays a critical role in the design of compact heat exchangers. Typically, air-side resistance to heat transfer contributes between 80 and 90 percent of the total resistance to heat flow. Commonly, densely packed fins are used to increase the air-side surface area and also play the dual role of increasing the heat transfer coefficient. This is accomplished by using various topologies such that the thermal boundary layer is constantly regenerated either by interrupted surfaces and/or inducing self sustained flow oscillations. Wavy fins, offset strip fins, and louvered fins are common examples. An additional aspect which any design has to be sensitive to is the friction penalty of achieving enhanced heat transfer. Hence, surface topologies which maximize heat transfer augmentation with minimal friction penalty are sought.

Recently surfaces imprinted with dimples or concave indentations have been researched extensively. One of the early investigations was conducted by Afansayev et al. [1], who investigated the effect of applying shallow dimples ($\delta/D = 0.067$) on flat plates on the overall heat transfer and pressure drop for turbulent flow. Significant heat transfer augmentation (30–40%) at negligible pressure drop augmentation was reported. Since then a number of experimental investigations have been conducted for different dimple geometries yielding heat transfer augmentation

* Corresponding author.
E-mail address: dtafti@vt.edu (D.K. Tafti).
URL: http:www.hpcfd.me.vt.edu (D.K. Tafti).

0017-9310/$ - see front matter © 2007 Elsevier Ltd. All rights reserved.
doi:10.1016/j.ijheatmasstransfer.2007.09.013

Nomenclature

D	dimple imprint diameter
C_f	fanning friction coefficient
f	non-dimensional frequency based on mean velocity and fin pitch
g^{ij}	contravariant metric tensor
k	thermal conductivity
S	stream-wise pitch
P	span-wise pitch
H	channel height or fin pitch (characteristic length scale)
L_x	periodic length
$\vec{n}$	surface normal vector
Nu	Nusselt number
p	fluctuating, modified or homogenized pressure
Pr	Prandtl number
q''	constant heat flux on channel walls
Re_τ	Reynolds number based on friction velocity (u_τ)
Re_H	Reynolds number based on mean flow velocity
Q_x	flow rate in the streamwise direction
t	non-dimensional time based on u_τ and H
Time	Non-dimensional time based on u_b and H
$\vec{u}$	cartesian velocity vector
u_τ	friction velocity (characteristic velocity)
u_b	mean flow velocity
$\vec{x}$	physical coordinates
β	mean pressure gradient
δ	dimple depth
γ	mean temperature gradient
θ	fluctuating, modified or homogenized temperature
Ω	heat transfer surface area
$\vec{\xi}$	computational coordinates

Subscripts

b	bulk
D_h	based on the hydraulic diameter of the channel
H	based on channel height
o	smooth channel
t	turbulent parameters
τ	values based on friction velocity

Superscripts

$+$	wall coordinates
$*$	dimensional quantities

factors of about 2–2.5 with low frictional losses compared to other surfaces with flow turbulators [2].

Most experimental studies were conducted in the fully turbulent flow regime; the few low Reynolds number studies conducted were mainly concerned with flow visualization, which showed periodic and continuous shedding of a primary vortex pair from the central portion of the dimple, in addition to a secondary vortex pair shed from the span-wise edges of the dimple (Mahmood et al. [3], Ligrani et al. [4,5]). Heat transfer distribution and local Nusselt number variation on the dimpled surface showed the existence of a low heat transfer region in the upstream half of the dimple cavity followed by a high heat transfer region in the downstream half. Additional regions of high heat transfer were identified at the downstream rim of the dimple. A number of studies have reported significant heat transfer augmentation at low pressure drop penalty (Mahmood et al. [3], Ligrani et al. [5], Chyu et al. [6], Moon et al. [7], Burgess and Ligrani [8] and Ekkad and Nasir [9]).

Study of the different geometrical factors resulted in the conclusion that the channel height to dimple imprint diameter ratio (H/D) and the dimple depth to dimple imprint diameter ratio (δ/D) play a significant role in the heat transfer and flow structure inside the domain. Ligrani et al. [4] reported that as H/D decreased the secondary flow structures and flow mixing intensified. Nevertheless, Moon et al. [7] obtained almost a constant heat augmentation ratio of 2.1 for a dimpled passage with $H/D = 0.37$, 0.74, 1.11 and 1.49, but their experiments were conducted in the fully turbulent flow regime ($Re \sim 12{,}000$–$60{,}000$). Burgess and Ligrani [8] reported that both Nusselt number and friction augmentation increased as (δ/D) increased.

The use of two dimpled surfaces on opposite walls was studied by Borisov et al. [10], where highest heat transfer enhancement was reported at $Re \approx 2500$. The use of dimples on rotating channel surfaces has been studied by Griffith et al. [11] who reported a heat transfer augmentation of 2.0. The effect of using spherical dimples and protrusions on opposite walls of the channel was studied by Ligrani et al. [12] and Mahmood et al. [13], where only the dimpled side of the channel was heated. Intensified secondary flow structures, flow unsteadiness and heat transfer augmentation were reported. Moon et al. [14] studied the effect of gap clearance in a channel with protrusions only on one side of the channel, where heat distribution showed high heat transfer augmentation at the front of the protrusion and in the passage between protrusions.

Numerical study of the problem of dimpled channel flow was conducted by a number of researchers. Wang et al. [15], using laminar flow simulation, identified a symmetric 3D horseshoe vortex inside a single dimple. Lin et al. [16], Isaev and Leont'ev [17], Park et al. [18], Won and Ligrani [19] and Park and Ligrani [20] used steady state Reynolds Averaged Navier Stokes (RANS) modeling to study flow and heat transfer in dimpled channel in the turbulent regime. All of the RANS calculations were done in the fully turbulent flow regime. Patrick and Tafti [21] used Direct Numerical Simulations (DNS) and Large-Eddy Simulations (LES) to predict the heat transfer and friction coefficient augmentation in a channel with one dimpled

wall at low Reynolds numbers ($Re_H = 50$–2000). Elyyan et al. [22] used LES to predict heat transfer and flow structure in a channel with dimples and protrusions on opposite sides for a fully turbulent flow of $Re_H = 15{,}000$. Recently, Wang et al. [23] used DNS to study turbulent flows over dimpled surfaces in a channel for different dimple depths, diameter and densities. They used a mesh density of 128^3 in resolving 4–16 dimples in a channel.

The objective of this paper is to investigate the low to moderate Reynolds number flow regime typical of compact heat exchangers and beyond into the fully turbulent regime. Most of the experimental work available is in the fully turbulent regime at very high Reynolds numbers. The flow regime in the current paper spans laminar steady, transitional, and turbulent flow. The geometry of interest is a channel with dimples and protrusions on opposite walls which is a realistic representation of dimpled fins in a heat exchanger. The calculations presented here are unique in a number of respects: in extending the state-of-the-art in the application of DNS and LES to complex geometries; in investigating the transitional and low to moderate Reynolds number turbulence regime which has not been studied before for this geometry; and finally leading to an enhanced understanding of heat transfer augmentation over dimpled and protruding surfaces by identifying the spatio-temporal evolution of flow variables and structures.

2. Governing equations and computational model

The computational model assumes fully-developed flow and heat transfer and simulates a periodically repeating spatial unit. Both channel walls are heated by imposing a constant heat flux (q''^*) boundary condition. The governing flow and energy equations are non-dimensionalized by a characteristic length scale which is chosen to be the height of the channel or fin pitch (H^*), a characteristic velocity scale given by the friction velocity $u_\tau^* = \sqrt{\Delta \overline{P}_x^*/\rho^*}$, and a characteristic temperature scale given by $q''^* H^*/k$. The assumed periodicity of the domain in the streamwise or x-direction requires that the mean gradients of pressure and temperature be isolated from the fluctuating periodic components as follows:

$$\begin{aligned} P^*(\vec{x},t) &= P^*_{\text{in}} - \beta^* x^* + p^*(\vec{x},t) \\ T^*(\vec{x},t) &= T^*_{\text{in}} + \gamma^* x^* + \theta^*(\vec{x},t) \end{aligned} \tag{1}$$

On substitution into the Navier–Stokes and energy equations, the non-dimensional time-dependent equations in transformed coordinates $\vec{\xi} = \vec{\xi}(\vec{x})$ take the following conservative form[1]:

Continuity:

$$\frac{\partial}{\partial \xi_j}\left(\sqrt{g}U^j\right) = 0 \tag{2}$$

Momentum:

$$\begin{aligned} &\frac{\partial}{\partial t}\left(\sqrt{g}u_i\right) + \frac{\partial}{\partial \xi_j}\left(\sqrt{g}U^j u_i\right) \\ &\quad = -\frac{\partial}{\partial \xi_j}\left(\sqrt{g}(\vec{a}^j)_i p\right) + \frac{\partial}{\partial \xi_j}\left(\left(\frac{1}{Re_\tau} + \frac{1}{Re_{t_\tau}}\right)\sqrt{g}g^{jk}\frac{\partial u_i}{\partial \xi_k}\right) + \sqrt{g}\beta\delta_{i1} \end{aligned} \tag{3}$$

Energy:

$$\begin{aligned} &\frac{\partial}{\partial t}\left(\sqrt{g}\theta\right) + \frac{\partial}{\partial \xi_j}\left(\sqrt{g}U^j\theta\right) \\ &\quad = \frac{\partial}{\partial \xi_j}\left(\left(\frac{1}{PrRe_\tau} + \frac{1}{Pr_t Re_{t_\tau}}\right)\sqrt{g}g^{jk}\frac{\partial \theta}{\partial \xi_k}\right) - \sqrt{g}\gamma u_1 \end{aligned} \tag{4}$$

where $\vec{a}^i$ are the contravariant basis vectors[2], $\sqrt{g}$ is the Jacobian of the transformation, g^{ij} are the elements of the contravariant metric tensor, $\sqrt{g}U^j = \sqrt{g}(\vec{a}^j)_i u_i$ is the contravariant flux vector, $\bar{u}_i$ is the Cartesian velocity vector, and θ is the modified temperature. The non-dimensional mean pressure gradient β is assumed to be unity, whereas γ is calculated from a global energy balance as: $\gamma = q''\Omega/Re_\tau \; PrQ_x L_x$. More details about the modified fully-developed treatment can be found in Zhang et al. [24].

Re_{t_τ} is the inverse of the non-dimensional turbulent eddy-viscosity and is modeled by the Smagorinsky model as

$$\frac{1}{Re_{t_\tau}} = C_s^2(\sqrt{g})^{2/3}|\bar{S}| \tag{5}$$

where $|\bar{S}|$ is the magnitude of the resolved strain rate tensor given by $|\bar{S}| = \sqrt{2\overline{S_{ik}S_{ik}}}$. The Smagorinsky constant C_s^2 is obtained via the dynamic subgrid stress model [25]. The turbulent Prandtl number is assumed to have a constant value of 0.5 [26].

The governing equations for momentum and energy are discretized with a conservative finite-volume formulation using a second-order central difference scheme on a non-staggered grid topology. The Cartesian velocities, pressure, and temperature are calculated and stored at the cell center, whereas the contravariant fluxes are stored and calculated at the cell faces. A projection method is used for time integration. The temporal advancement is performed in two steps, a predictor step, which calculates an intermediate velocity field, and a corrector step, which calculates the updated velocity at the new time step by satisfying discrete continuity.

The computer program GenIDLEST (Generalized Incompressible Direct and Large-Eddy Simulations of Turbulence) used for these simulations has been applied extensively to study air-side heat transfer augmentation in compact heat exchangers, e.g. Cui and Tafti [27], and in stationary and rotating internal ducts used for cooling gas turbine blades, e.g. Sewall et al. [28], and other heat transfer

[1] Henceforth, all usage is in terms of non-dimensionalized values.

[2] The notation $(\vec{a}^j)_k$ is used to denote the kth component of vector $\vec{a}^j$. $(\vec{a}^j)_k = \partial\xi_j/\partial x_k$.

augmentation geometries with very close matches with experiments in the literature. Details about the algorithm, functionality, and capabilities can be found in Tafti [29].

3. Calculation of friction and heat transfer coefficients

Typically the calculations are initiated with some initial guess of the velocity and temperature field under the imposed pressure gradient and integrated in time till the flow and heat transfer adjust to the new conditions and reach a steady state. In the unsteady regime the velocity and temperature fields are integrated further to obtain statistical means. Typical sampling times are 5–15 non-dimensional time units. The mean fields are then used to present time-averaged data. All results are non-dimensionalized by the mean flow velocity u_b and fin pitch H.

To characterize the heat transfer, we define a local Nusselt number based on channel height as

$$Nu = \frac{H^* q''^* / (T_s^* - T_{ref}^*)}{k^*} \tag{6}$$

where T_s^* and T_{ref}^* are the dimensional surface temperatures (time-mean when unsteady flow) and global reference temperature, respectively. In terms of non-dimensional quantities the above can be re-written as

$$Nu = \frac{1}{\theta_s - \theta_{ref}} \tag{7}$$

where θ_s is the local modified non-dimensional surface temperature and θ_{ref} is the reference modified non-dimensional temperature defined as:

$$\theta_{ref} = \frac{\int\int |u| \theta \mathrm{d}A_x}{\int\int |u| \mathrm{d}A_x} \tag{8}$$

The surface-averaged Nusselt number is obtained by integration over the protrusion and dimple surface as:

$$Nu = \frac{\int\int \mathrm{d}S}{\int\int (\theta - \theta_{ref}) \mathrm{d}S} \tag{9}$$

where S denotes the heat transfer surface.

The Fanning friction coefficient C_f is calculated as:

$$C_f = \frac{(\overline{\Delta p}^* / L_x^*)(D_h^*)}{2\rho^* \cdot u_b^{*2}} \tag{10}$$

After substituting the non-dimensional value of $\overline{\Delta p}/L_x$ as unity, the expression reduces to

$$C_f = \frac{D_h}{2u_b^2} \tag{11}$$

where u_b is the bulk mean flow velocity obtained from the simulation under the condition of the applied mean pressure gradient of unity. D_h is the hydraulic diameter and its usual definition yields $D_h = 1.8263$ for both cases[3].

[3] For a plain channel, $D_h = 2$. However, the dimple and protrusion increase the wetted perimeter by a factor of 1.095 for both cases.

The heat transfer and friction augmentation ratios are calculated based on baseline values. In the present study, the laminar Fanning friction coefficient and Nusselt number for flow between smooth parallel plates and the Petukhov and Gnielinski correlations for turbulent flow are used to calculate the baseline Fanning friction coefficient and Nusselt number, respectively [30]. The choice of correlations was made based on their validity and accuracy over the range of Reynolds numbers of interest in this study. The friction coefficient and Nusselt number for these correlations based on Re_H are as follows:

$$\begin{aligned}
C_{f_0} &= \frac{12}{Re_H}; \quad Re_H < 1500 \\
C_{f_0} &= (1.580 \ln Re_H - 2.185)^{-2}; \quad 1500 \leqslant Re_H \leqslant 2.5 \times 10^6 \\
Nu_0 &= \frac{hH}{k} = 4.12; \quad Re_H < 1500 \\
Nu_0 &= \frac{(C_{f_0}/2)(Re_H - 500)Pr}{1 + 12.7(C_{f_0}/2)^{1/2}(Pr^{2/3} - 1)}; \quad 1500 \leqslant Re_H \leqslant 2.5 \times 10^6
\end{aligned} \tag{12}$$

Although the original forms of the equations are in terms of Re_{D_h}, they are rewritten here in terms of Re_H assuming that for a smooth channel $D_h^* = 2H^*$.

4. Fin geometry

The fin geometry consists of two parallel plates with staggered dimples and protrusions on opposite walls without any offset with respect to each other, as shown in Fig. 1a. Table 1 summarizes the two geometries tested. In Case 1, the non-dimensional span-wise and stream-wise pitches are $P = S = 1.62$, and the dimple imprint diameter, $D = 1.0$, with dimple depth, $\delta = 0.2$. In Case 2, all the dimple dimensions are doubled with respect to the fin pitch or channel height. Physically, this is representative of a scenario in which the dimensional fin pitch is decreased by a factor of two while keeping the physical dimensions of the dimple imprint geometry the same or conversely keeping the fin pitch the same and increasing the dimple dimensions by a factor of two. Case 2 matches the experimental set up of Mahmood et al. [13].

5. Domain size and grid resolution

Under the assumption of fully-developed flow and heat transfer, it is desirable to choose the smallest repetitive unit as the computational domain to minimize the computational cost. Moreover, the selected computational domain should be capable of capturing all the relevant physical modes in the solution. If the imposed periodicity is too small a spatial domain, the important modes pertinent to the solution will not be captured. To investigate the trade-off between computational cost and accuracy, an initial study is conducted to investigate the effect of domain size on the solution. The smallest periodic domain which

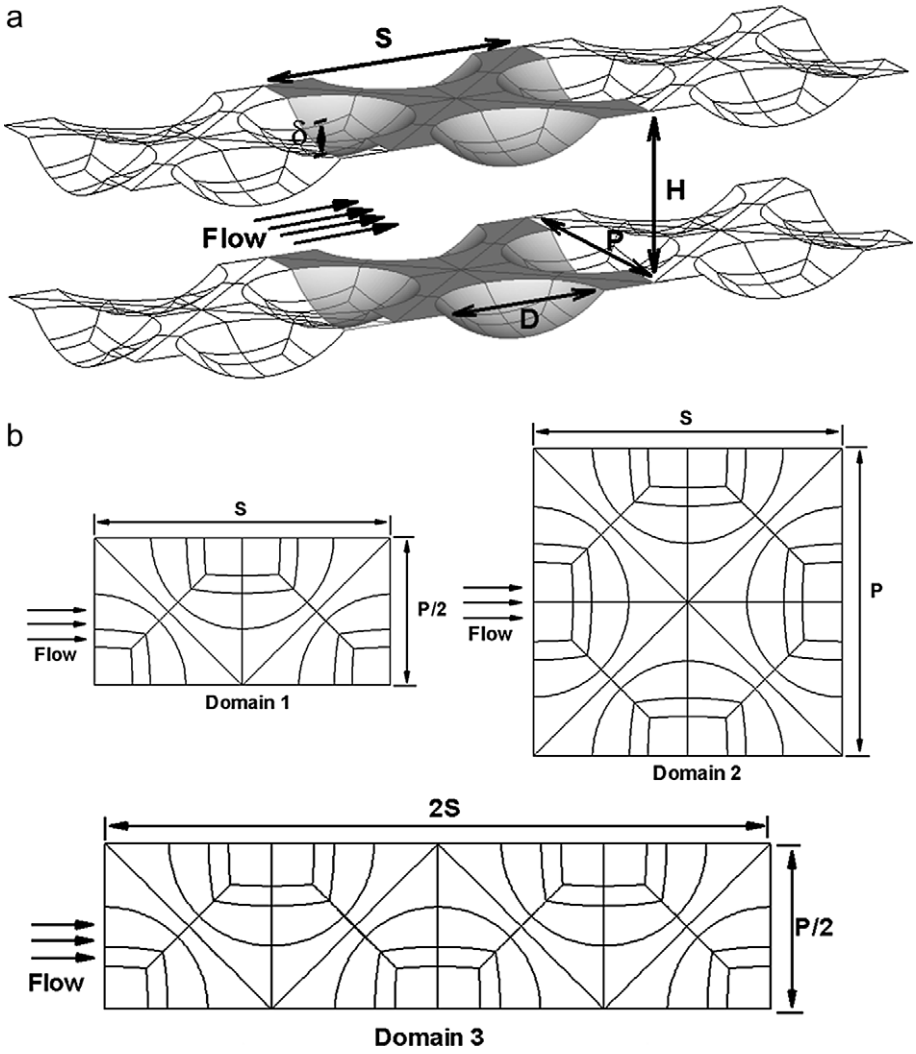

Fig. 1. (a) Dimpled channel geometry and (b) different computational domain sizes: Domains 1, 2 and 3.

Table 1
Non-dimensional geometry specifications

	$H = H^*/H^*$	$D = D^*/H^*$	$\delta = \delta^*/H^*$	$P = P^*/H^*$	$S = S^*/H^*$
Case 1	1.0	1.0	0.2	1.62	1.62
Case 2	1.0	2.0	0.4	3.24	3.24

can be constructed is Domain 1 ($1 \times P/2 \times S$) as shown in Fig. 1b, whereas Domain 2 ($1 \times P \times S$) and Domain 3 ($1 \times P/2 \times 2S$) admit lower wave number solutions in the stream-wise and span-wise directions. The domains and grid sizes with friction and heat transfer augmentation results are summarized in Table 2 at $Re_H = 3700$ for Case 1.

The results in Table 2 show a difference of less than 3% between Domain 1 and 2 and less than 5.6% between Domains 1 and 3, in time-averaged Nusselt number and friction coefficient augmentations and hence Domain 1 was deemed adequate to accurately represent the physics of the flow and heat transfer.

Table 2
Effect of domain size on solution

Domain	1	2	3
Dimensions	$1 \times P/2 \times S$	$1 \times P \times S$	$1 \times P/2 \times 2S$
# of cells	933,888	1,867,776	1,867,776
Re_H	3735	3714	3826
Nu/Nu_o	2.72	2.67	2.57
% Difference	*Reference*	1.5	5.55
C_f/C_{f_0}	4.87	4.94	4.70
% Difference	*Reference*	1.5	3.5

A hybrid structured/unstructured multi-block grid is used to discretize the computational domain with a total mesh resolution of approximately 933 thousand computational cells for Case 1 and 1.6 million cells for Case 2. The grid is designed such that maximum resolution is provided in the dimple (protrusion), and in the vicinity of the top and bottom surfaces. In the wall normal direction the first grid point is placed at $\Delta \approx 6.5 \times 10^{-4}$ near the two channel walls. An *a-posteriori* calculation of the local

friction velocity for Case 2 at the highest Reynolds number showed that the condition $y_1^+ < 1$ is satisfied throughout on both surfaces [22]. In addition, surface-averaged values of the wall parallel distribution is $\Delta_{//}^+ \approx 15$ at the highest Reynolds number simulated.

In the two geometries, the laminar to unsteady laminar regimes are treated in a direct simulation mode without any subgrid model. The LES model is only activated after the flow tends towards a chaotic turbulence like regime which for Case 1 is at $Re_H = 1000$ and for Case 2 at $Re_H = 700$. It is noted that the dynamic model calculates a physically correct eddy-viscosity based on the grid resolution and the turbulence length scales present in the flow. From previous calculations on similar mesh resolutions for a dimpled channel [31], the subgrid modeling is expected to have a negligible effect on mean heat transfer and friction at least up to $Re_H = 2000$.

6. Validation

For the purposes of this study, a calculation was conducted to compare with the experimental data of Mahmood et al. [13]. The experimental setup was similar to Case 2 with the exception that only the dimpled surface was heated. To replicate the experimental conditions, a constant heat flux boundary condition is applied to the dimpled surface and an adiabatic wall boundary condition is applied to the protrusion surface in the calculation. The Reynolds number based on the channel height, Re_H, is 14,600.

Table 3 summarizes the comparisons. While the Nusselt number augmentation shows excellent agreement with experiments, the augmentation of C_f is more than twice the value reported by Mahmood et al. [13]. To further investigate this discrepancy, a calculation was conducted for a channel with dimples on one side and a smooth wall on the other at $Re_H = 8160$. The Nusselt number augmentation obtained by the calculation ($Nu/Nu_o = 1.69$) compared well with the experimental value of ($Nu/Nu_o = 1.83$) reported by Mahmood et al. [13] at $Re_H = 10200$. The predicted friction coefficient augmentation of $C_f/C_{f_0} = 2.67$, on the other hand, was much higher than the value of 1.50 reported in [13]. The good match in Nusselt number augmentation ratio but the large irreconcilable difference in friction augmentation is puzzling. The same computational techniques have been used in ribbed duct flows to obtain friction augmentation in very close agreement with experiments [28]. Additionally, computations in turbulent channel flow at $Re_H = 5600$ show excellent agreement with friction and Nusselt number correlations (within 5–10%) [22].

Table 3
Comparison between numerical and experimental results

	Re_H	Nu/Nu_o	C_f/C_{f_0}
Present study	14,600	2.31	6.36
Experimental [13]	15,000	2.23	3.08

7. Results and discussion

7.1. Laminar flow and transition to turbulence

This section describes the typical mean flow features in the laminar regime and the transition to turbulence. For the two geometries investigated, Case 1 and Case 2, Fig. 2 plots 3D streamlines injected near the dimple and protrusion surfaces at nominal $Re_H = 250$. In both cases the flow is laminar at this Reynolds number. At the dimpled surface the flow accelerates as it approaches the upstream edge of the dimple where it separates forming a recirculating zone in the dimple. The recirculating zone extends to the downstream edge of the dimple where the separated shear layer reattaches. Upon reattachment, the flow accelerates upward along the downstream rim of the dimple. Part of the recirculating flow, as it traverses the side of the dimple, decelerates, loses momentum and is ejected along the side rims. On the other side of the channel, the flow accelerates around and on the protrusion. The flow on the protrusions accelerates up to an angle of 70–80° after which it decelerates up to 180°; at low Reynolds number no separation in the wake is observed.

To identify the coherent vorticity in the present study, the vortex eduction technique proposed by Chong et al. [33]. In this method, in regions dominated by vortical motion, the velocity gradient tensor exhibits two eigen values which are complex conjugates. The magnitude of the eigenvalue is indicative of the strength of the vortex. The structures identified by this method are referred to as "coherent vorticity" in this paper, and the magnitude of the eigenvalue as the strength of the coherent vortices.

Fig. 3 shows isosurfaces of coherent vorticity near the dimple and protrusion surface as a function of Reynolds number, and the corresponding velocity traces near the surface on the flat landing downstream of the dimple and in the wake of the protrusion for Case 1. The beginning of transition to turbulence is signaled by the break in symmetry of the 3D vorticity. On the dimple, coherent vorticity is generated at the upstream and downstream rims, which is mostly the agglomeration of spanwise or z-directional vorticity. On the protrusion side, the calculated coherent vorticity is concentrated between protrusions, and at the leading side of the protrusion in regions of high flow acceleration. In Case 1, a slight asymmetry is observed as early as $Re_H = 530$ on the protrusion side of the channel (not shown). However, the developing instability is not reflected in the velocity signal in the wake of the protrusion. At $Re_H = 790$, the asymmetry gets stronger and the velocity in the wake of the protrusion and immediately downstream of the dimple show a periodic fluctuation. This is in spite of the fact that the coherent vorticity distribution at the dimple shows no visible asymmetry. Hence it is concluded that for Case 1, the asymmetry which eventually leads to transition to turbulence develops in the wake of the protrusions and spreads to the rest of the domain. By $Re_H = 990$, the asymmetry spreads to the dimples as well and the flow is

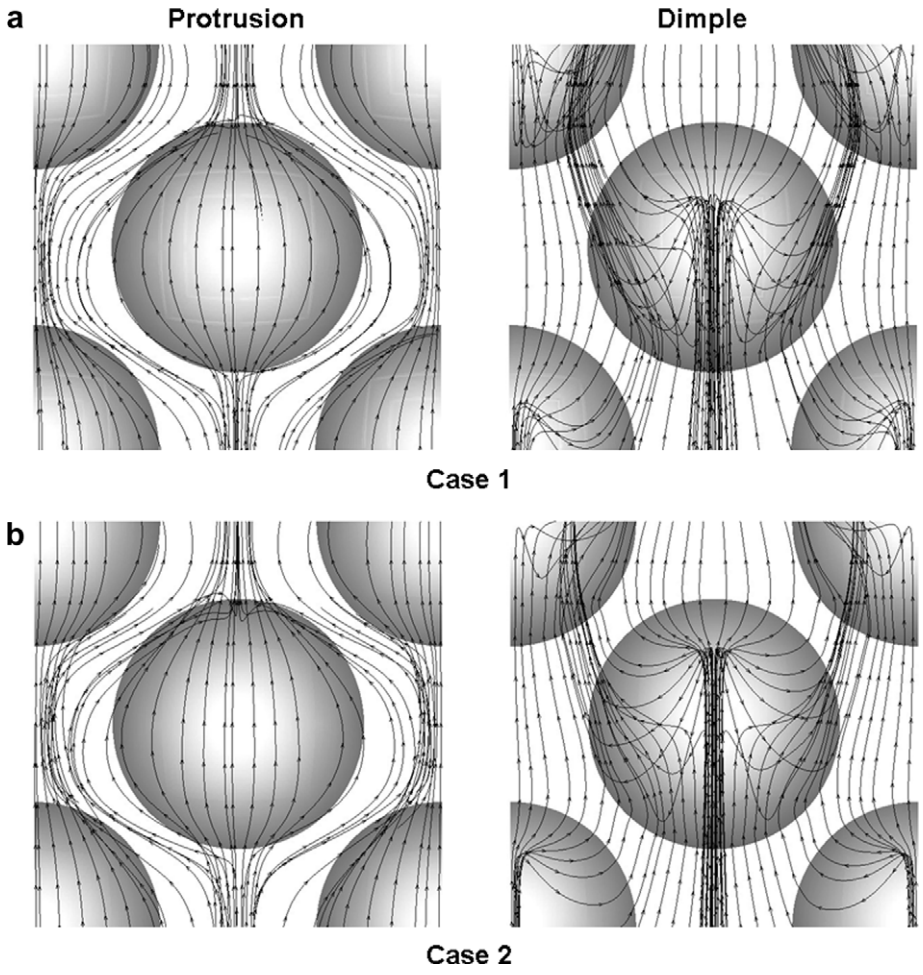

Fig. 2. Mean 3D velocity streamlines in laminar flow at nominal Re_H of 250.

well into the transitional regime with highly fluctuating and somewhat intermittent signal.

For Case 2, the structure of coherent vorticity is noticeably different in the dimple (Fig. 4). In this case, the initial asymmetry in the flow appears earlier in the dimple. This is inferred from the signal downstream of the dimple on the flat landing at $Re_H = 440$, which exhibits a sinusoidal low amplitude variation, although no visible asymmetries are found in the vorticity distribution on both sides. By $Re_H = 480$, the flow on both sides exhibits a chaotic structure. Hence, Case 2 with a larger dimple depth and imprint diameter transitions much earlier than Case 1. However the transition to turbulence is more gradual and is not as sharp as that observed in Case 1.

7.2. Turbulent flow regime

In the fully turbulent regime ($Re_H = 15{,}000$), Fig. 5, the mean flow streamlines show the existence of two vortical structures, which together form the recirculation region inside the dimple cavity. These recirculation zones are symmetrical about the dimple center-plane and the core of each structure is located in the upstream half of the dimple. As the flow Reynolds number increases the size of the recirculation zone shrinks; this is due to early reattachment of the flow as the separated shear layer becomes more turbulent. Between the two cases, Case 2 has a noticeably smaller reattachment length. It is observed that as the flow ejects from the dimple, the rim curvature induces helicity to the mean streamlines around the downstream rim of the dimple, which manifests instantaneous helical vortices shed from the rim. On the protrusion, the flow accelerates on the leading face and on deceleration leads to 3D separation with a highly unsteady wake. The boundary layer on the protrusion separates earlier in Case 1. Additionally, another small recirculation region just upstream of the protrusion can be identified as the flow slows down before it impinges on the front of the protrusion.

7.3. Coherent vorticity structure and magnitude

Coherent vortical structures and dynamics play an important role in heat transfer enhancement [32]. A single-valued isosurface (value 10) of coherent vorticity is shown in Fig. 6 for nominal $Re_H = 1400$ on the dimple and protrusion side of the channel. Comparing the density

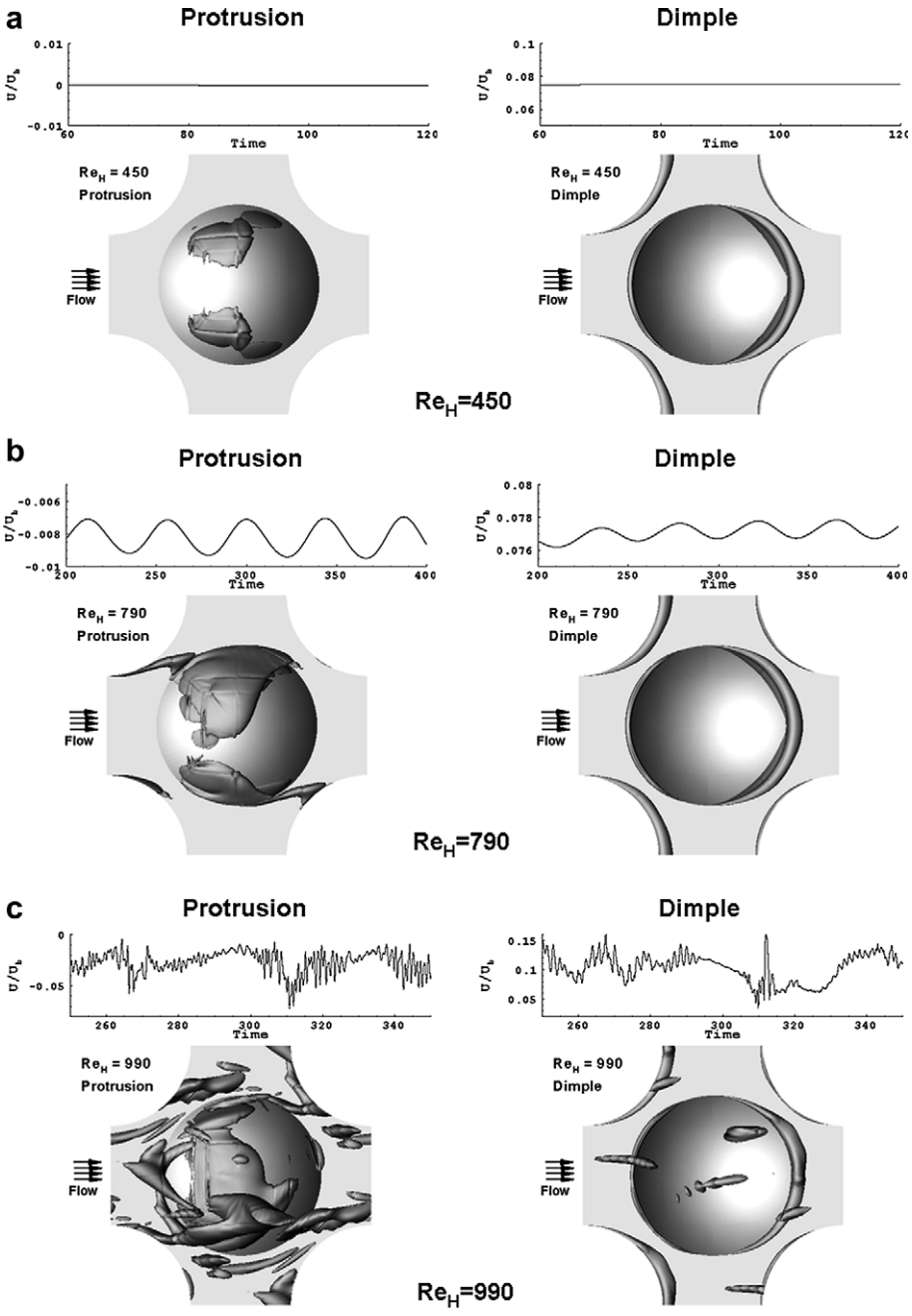

Fig. 3. Isosurfaces of the coherent vorticity for Case 1 with isosurface level = 10.

of the educed structures between Cases 1 and 2, it is evident that Case 2 contains more turbulent eddies than does Case 1, particularly on the dimple side of the channel. Although difficult to decipher in these snapshots, vorticity shed from the separated shear layer in the dimple is ejected out from the reattachment region in the dimple cavity. On ejection, the vortices are stretched and tilted in the stream-wise direction as they come in contact with the mainstream flow and are transported in the close vicinity of the flat landing downstream of the dimple. Additional vorticity is also generated as the flow ejects out over the side and downstream rims of the dimple cavity. On the protrusion side of the channel, vorticity is mainly shed from the separated shear layers which form the wake vortices. These observations on the flow dynamics in the dimple cavity generally agree with the flow visualization observations made by Won et al. [34].

As the Reynolds number increases and the flow becomes more turbulent, the magnitude of the coherent vorticity also increases. Since the coherent vorticity in the domain is closely linked to the level of heat transfer enhancement [32], it is useful to find a means of quantifying the variation of the coherent vorticity with Reynolds number in the calculation domain. This is done by defining a volume-weighted

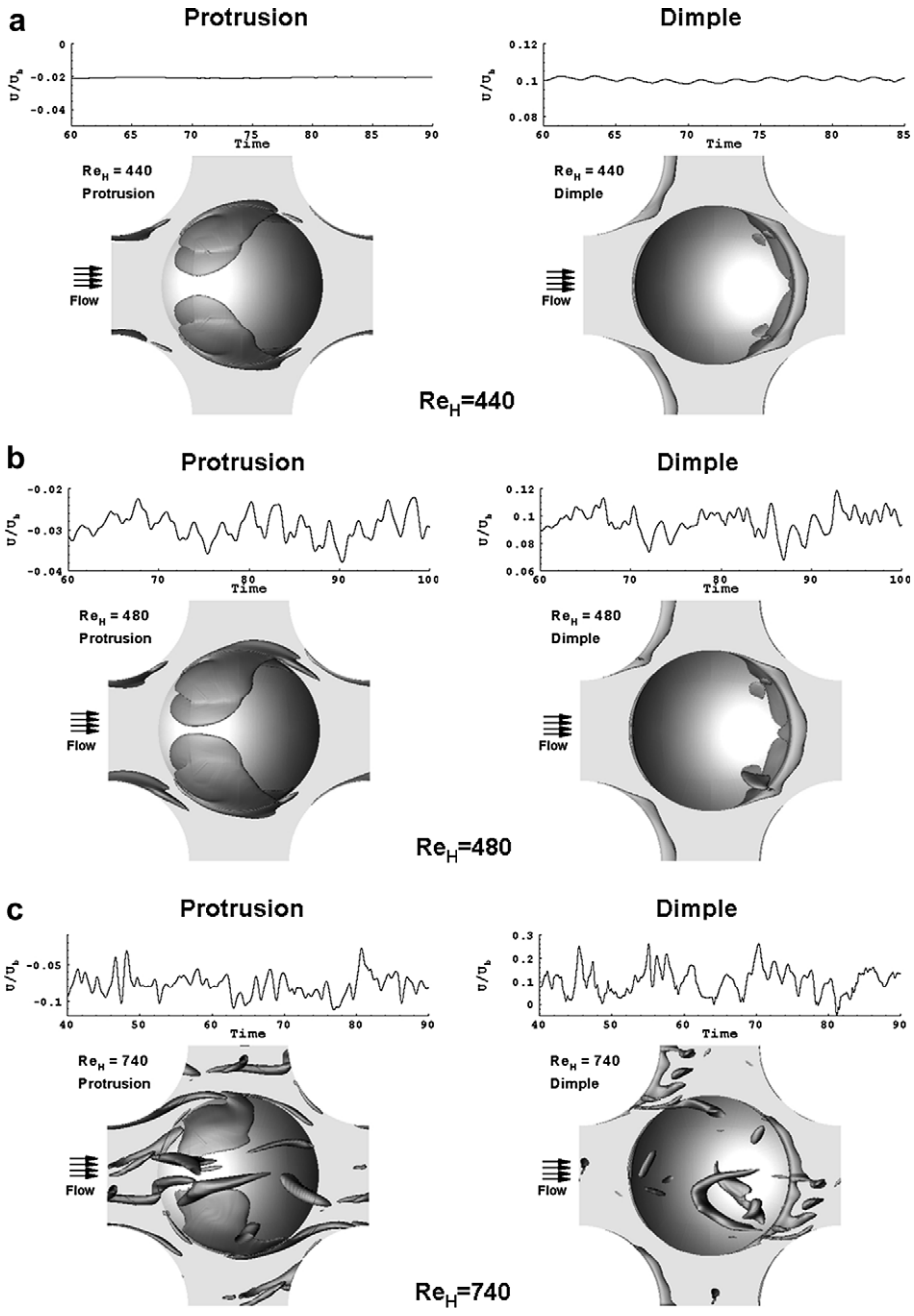

Fig. 4. Isosurfaces of the coherent vorticity for Case 2 with isosurface level = 10.

time-averaged coherent vorticity (Ψ) in the domain, which is calculated by finding the time-mean of the instantaneous coherent vorticity and then finding the volume average of that quantity over the whole calculation domain. This is plotted in Fig. 6c and shows that the time-mean volume averaged coherent vorticity increases with Reynolds number and that it is higher in Case 2 than in Case 1 up to a Reynolds number of 2000, after which both geometries exhibit very similar magnitudes. For Case 1, there is a sharp increase in coherent vorticity as the flow transitions to turbulence, whereas Case 2 exhibits higher values for $Re_H < 1000$, which increase gradually as the flow Reynolds number increases.

7.4. Turbulent kinetic energy and turbulent statistics

Fig. 7 shows the Turbulent Kinetic Energy (TKE) normalized by the square of the mean velocity, at a span-wise plane located at 0.2 D downstream of the edge of the dimple and a stream-wise plane at the centerline of the dimple/protrusion. Regions of high TKE values are observed:

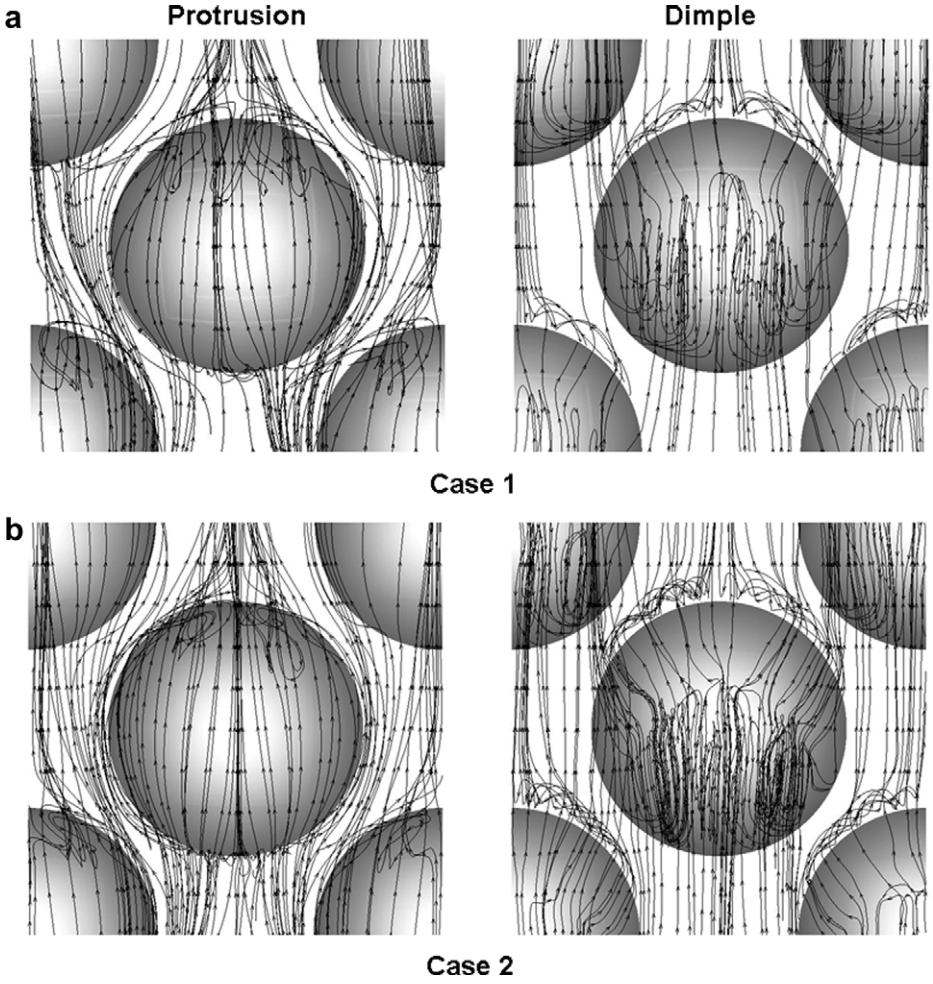

Fig. 5. Mean flow structures in turbulent flow, at nominal $Re_H = 15{,}000$, for protrusion (left) and dimple (right) for: (a) Case 1 and (b) Case 2.

- In the separated shear layer in the dimple where the mainstream flow and recirculation region interact.
- Close to the flat landing downstream of the dimple, due to the reattachment of the small scale vortices ejected from the dimple cavity.
- In the wake of the protrusion.

While Case 1 exhibits slightly higher levels of TKE in the wake of the protrusion (possibly a result of the smaller wake region in Case 2), the TKE levels on the dimple side are noticeably higher for Case 2 in the separated shear layer and at the flat landing behind the dimple. This is attributed to the larger dimple depth and the more intense vorticity generated in the dimple cavity.

Fig. 8 shows the effect of Reynolds number on the TKE profile at a span-wise center-plane through the dimple located at 0.2 D downstream of the edge of the dimple/protrusion. Two major conclusions can be made from these profiles, which are: (i) There is a large increase in TKE levels near the respective channel surfaces in the wake of the protrusion and on the flat landing behind the dimple as the Reynolds number increases beyond $Re_H \approx 1400$. The shift in the location of the peak value of TKE on the protrusion side is a result of early separation at low Reynolds numbers which displaces the wake away from the surface. Between $Re_H = 9000$ and 15,000, the normalized profiles of TKE are quite similar indicating no change in the turbulent structure of the flow. (ii) As observed earlier, the TKE level near the flat landing for Case 2 is substantially higher than Case 1. However, there is no substantial difference between the two cases on the protrusion side, indicating that the increased depth of the protrusion does not have any effect on the wake structure, whereas the increased depth of the dimple produces more turbulence.

Fig. 8c shows the variation of volume averaged TKE with Reynolds number much like the volume averaged coherent vorticity plotted in Fig. 6c. It is observed that Case 2 exhibits higher values than Case 1 over the full range of Reynolds numbers. However, it is noteworthy that while the normalized TKE asymptotes to a near constant value after $Re_H = 4000$ for Case 1 and $Re_H = 2000$ for Case 2, the normalized coherent vorticity keeps increasing with Reynolds number, which as will be shown later correlates much better with the Nusselt number variation.

Fig. 9 shows representative component RMS profiles of the fluctuating velocities for Case 2 at the same location as

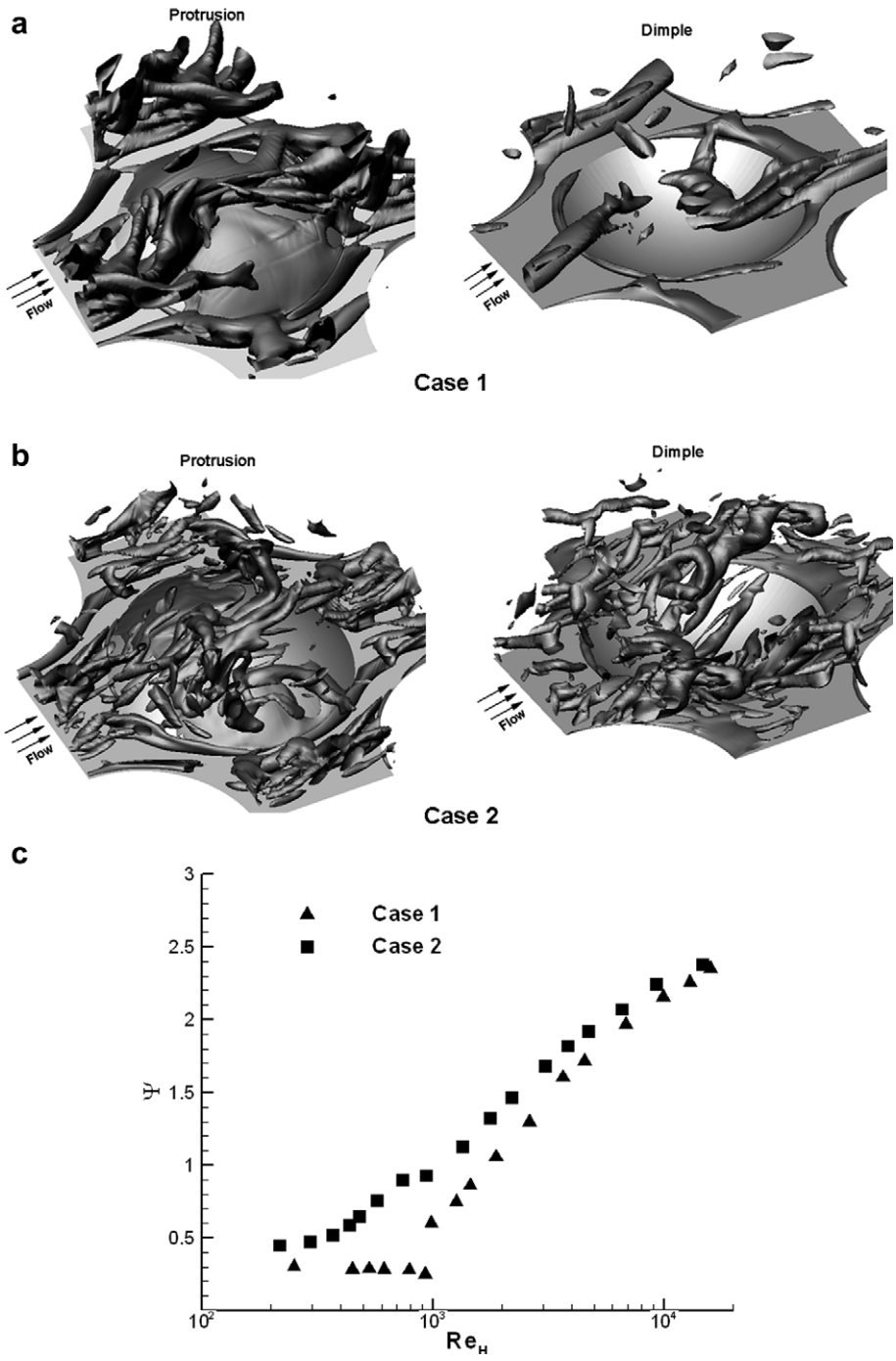

Fig. 6. Isosurfaces of coherent vorticity (level = 10) at nominal $Re_H = 1400$ for: (a) Case 1; (b) Case 2 and (c) volume-weighted time-averaged coherent vorticity (Ψ).

that in Fig. 8. Near the walls on the dimple side, the turbulent energy is dominated by the U_{rms} component, which results from the streamwise fluctuations produced by the small scale vorticity ejected from the dimple as well as that produced by the shear layer around the rim of the dimple. On the protrusion side, turbulent energy is highest in the W_{rms} component, which is a result of the highly unsteady lateral entrainment into the low pressure wake behind the protrusion. The three components exhibit isotropy in the middle half of the channel but strong anisotropies are present in the distributions near the surfaces.

7.5. Friction characteristics

Both friction drag and form or pressure drag contribute to the overall frictional losses. Fig. 10a shows the contribution of form drag and friction drag to the total drag in the channel as a function of Reynolds number for both

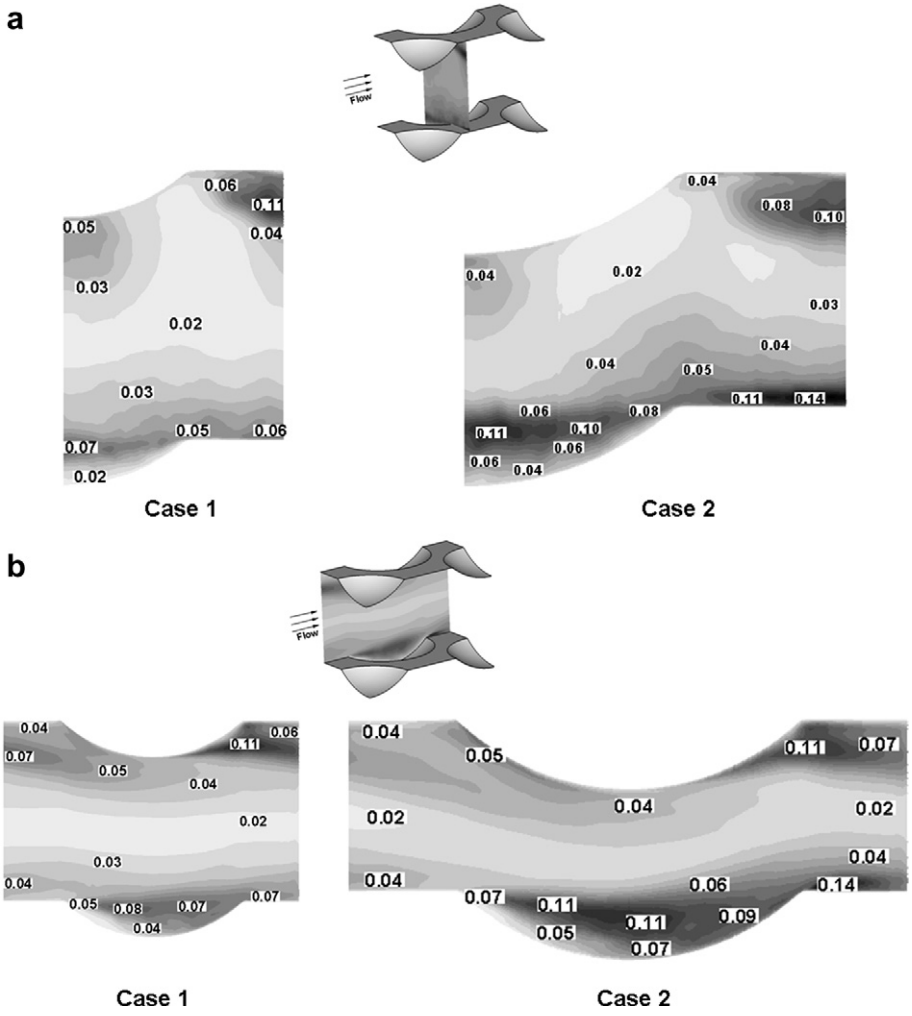

Fig. 7. Normalized TKE distribution, at nominal $Re_H = 15{,}000$, on: (a) cross sectional cut at 0.2D downstream the dimple edge and (b) stream-wise cut across the centerline of the domain.

geometries. In the laminar regime, the pressure differential across the protrusion is small in the absence of separation. In the dimple cavity, the pressure differential between the fore and aft side of the dimple is also small. Hence, at low Reynolds numbers the shear or surface friction dominates the total losses. As the Reynolds number increases and flow separation and wake formation on the protrusion and separation and reattachment within the dimple intensify, form losses start dominating over surface friction. The trend is present in both geometries, except that the transition from a friction dominated pressure drop to a form dominated one occurs much earlier in Case 2 ($Re_H = 400$) than in Case 1 ($Re_H = 1200$) and seems to be correlated to the onset of unsteadiness in the two geometries. At Reynolds numbers above 10,000, the percentage form and friction drag asymptote to a near 80–20 split.

Fig. 10b shows a further breakdown of the percentage contribution of form and friction drag on the dimple and protrusion surfaces for the two cases. The protrusion surface exhibits a distinct cross-over between form and friction drag at $Re_H = 1500$–2000 for both cases. The dimple surface, on the other hand, behaves differently. Whereas Case 1 shows the crossover at $Re_H = 1000$, the crossover for Case 2 occurs at a much lower Reynolds number. These observations lead to the conclusion that the losses on the dimpled surface are much more dependent on the onset of unsteadiness than the surface with protrusions. It is also noted that in both cases, form losses on the dimple surface are larger than form losses on the surface with protrusions. While form losses on the protrusion surface assume fairly constant values beyond $Re_H = 5000$, the corresponding form losses on the dimple side exhibit a steady increase with Reynolds number. This can be explained by postulating that the protrusion wake dynamics (scaled by ρu_b^2) becomes Reynolds number independent much quicker than the dynamics of separation and reattachment in the dimple, which is the primary contributor to form losses in the dimple. In fact, the asymptotic nature of form drag with Reynolds number agrees with the constancy of drag coefficients for flow over bluff bodies. While the percentage form drag on the dimple side is larger in Case 2 than in Case 1, it is noteworthy that on the protrusion side, Case 1 exhibits a

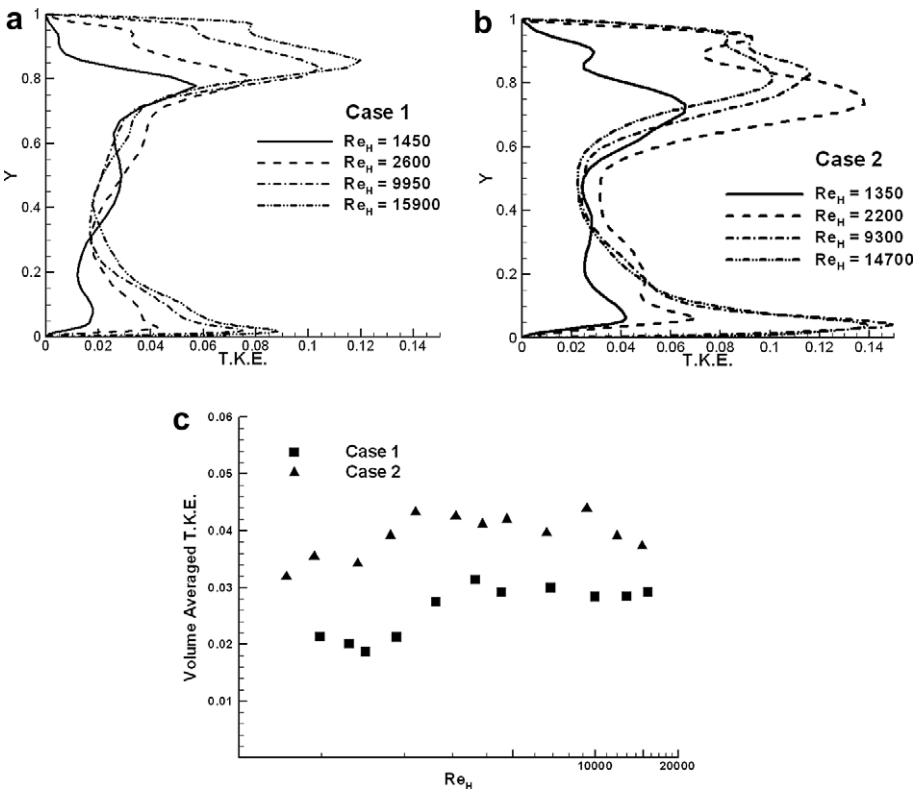

Fig. 8. Profile of TKE at 0.2D downstream of the dimple on the centerline for: (a) Case 1; (b) Case 2; and (c) volume averaged TKE variation with Re_H for both cases.

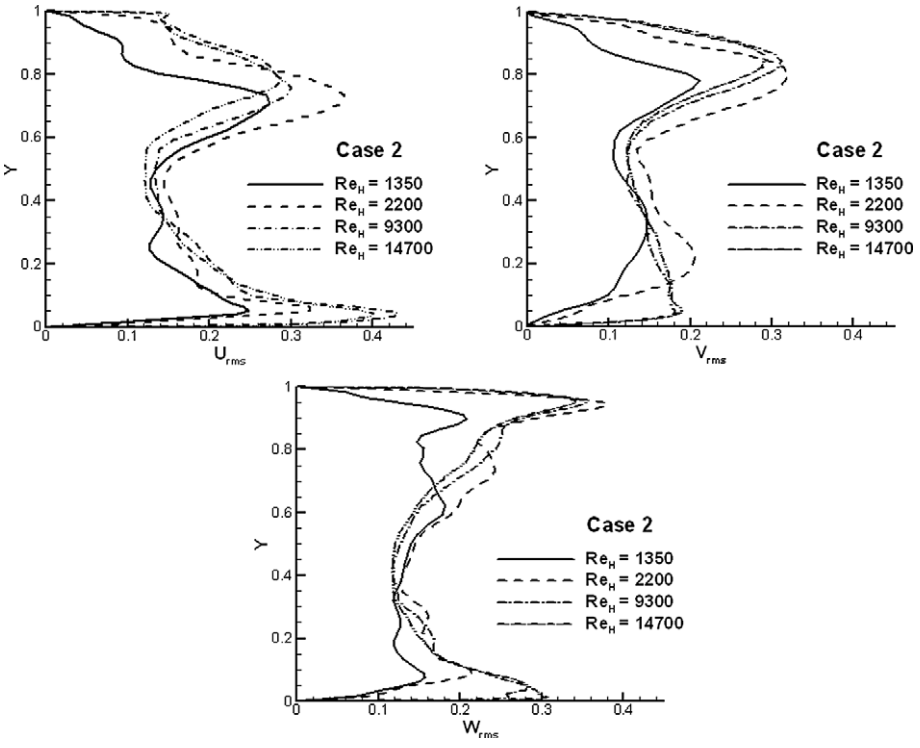

Fig. 9. RMS profiles 0.2D downstream of the dimple on the centerline for Case 2.

higher percentage form contribution to the total drag, in spite of a larger protrusion in Case 2. This can be attributed to the formation of a smaller wake in Case 2 (see Fig. 5).

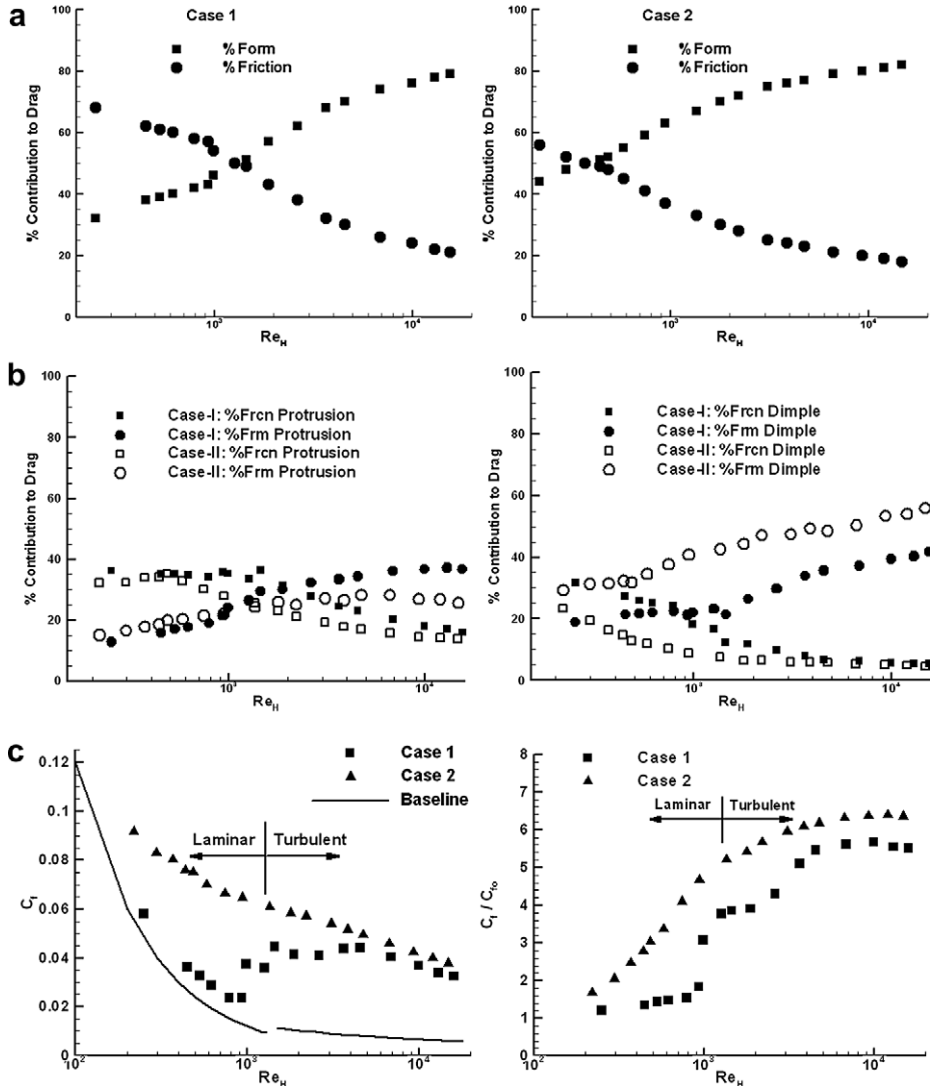

Fig. 10. Variation of form and friction drag contribution to overall pressure losses. (a) Percentage form and friction contribution to overall losses; (b) breakdown of contributions from dimple and protrusion surface and (c) variation of friction coefficient and augmentation ratio with Reynolds number.

Fig. 10c shows the variation of the friction coefficient and its augmentation over a smooth plain channel with Reynolds number. Case 2 exhibits higher friction coefficients at low to moderate Reynolds numbers in the laminar and early turbulence regime but on the onset of turbulent flow in Case 1, the two friction coefficients are comparable to each other. A striking feature of Case 2 is that there is no well defined transition from laminar to turbulent flow in the friction coefficient, much like the variation in the time-mean volume averaged coherent vorticity (Ψ) in Fig. 6c. Rather the friction coefficient behaves much like that in a turbulent flow even at low Reynolds numbers. This behavior is consistent with observations on the onset of instabilities which occur as early as $Re_H = 440$, but which develop much more gradually than Case 1. On the other hand Case 1 exhibits a classical shape with a distinct laminar region followed by transition and a fully turbulent region. Up to a $Re_H = 1000$, C_f in Case 1 behaves much like that in a plain channel flow with augmentation ratios ranging from 1 to 1.4, which increases to about 5.5 at $Re_H = 10{,}000$.

7.6. Heat transfer characteristics

Fig. 11 shows the Nusselt number augmentation distribution on the dimple and protrusion surfaces for laminar flow at nominal $Re_H = 250$ and turbulent flow at nominal $Re_H = 15000$. At $Re_H = 250$ on the protrusion side, the heat transfer coefficient attains a maximum at the apex of the protrusion for Case 1, where the flow reaches its maximum velocity as it accelerates on the front half of the protrusion. For Case 2, the region of augmentation spreads to the sides of the protrusion due to the larger flow acceleration experienced between adjacent protrusions. At the same time, the flat landing in the wake of the protrusion exhibits a more pronounced deterioration in the Nusselt number for Case 2. On the dimple side, Case 2 shows higher overall heat transfer augmentation within the dimple cavity,

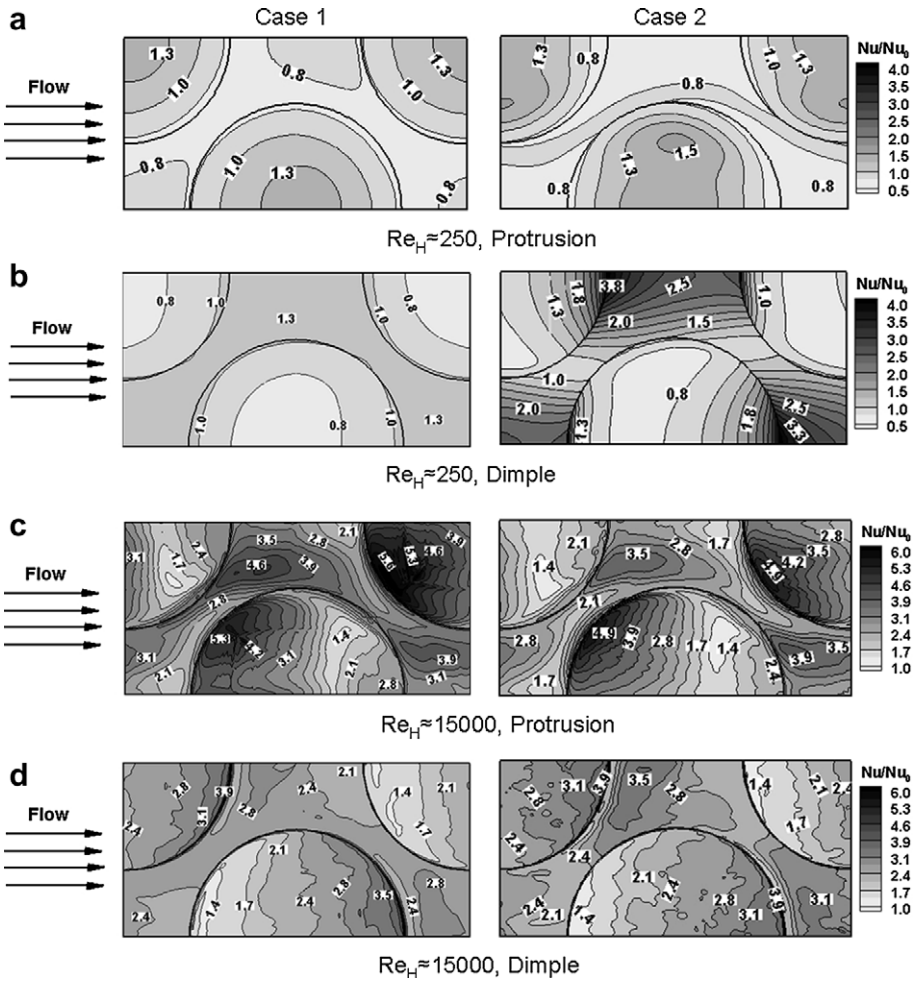

Fig. 11. Distribution of Nusselt number augmentation.

because of the smaller recirculation region. Larger augmentation is also noticed on the flat landing downstream of the dimple, which is influenced by the stronger flow ejection out of the deeper cavity.

The augmentation pattern on the dimple side remains the same as the Reynolds number increases to $Re_H \approx 15{,}000$; but changes considerably on the protrusion side. The maximum augmentation shifts to the fore-sides of the protrusion as the bulk of the flow now accelerates around the sides of the protrusions. An additional zone of high augmentation is found in the wake of protrusion where the separated shear layer on the protrusion comes in the proximity of the flat landing. Regions of low heat transfer are observed on the flat landing in front of the protrusion due to the development of secondary recirculation regions. Whereas Case 1 has a higher heat transfer augmentation on the protrusion side compared to Case 2, the opposite trend is observed on the dimple side. Within the dimple cavity, regions of low heat transfer shrink considerably as the flow becomes turbulent. For Case 2 at $Re_H \approx 15{,}000$ a small zone of low heat transfer appears along the downstream rim of the dimple as a result of the recirculation region that forms as the flow ejects out of the dimple cavity. The heat transfer augmentation reaches another maximum as the flow reattaches to the fin surface at the flat landing downstream of the dimple.

Fig. 12 plots the variation of area-weighted time-averaged Nusselt number with Reynolds number. Case 2 clearly shows higher heat transfer coefficients up to $Re_H = 1000$. The higher Nusselt numbers is a result of the earlier onset of unsteadiness in Case 2 combined with the more intense flow impingement and acceleration on the protrusion. In this range, Case 1 shows little or no augmentation till the flow develops instabilities and transitions to turbulence. It is clear from these results that between the two geometries, Case 2 is more viable for heat transfer augmentation in the low Reynolds number range less than $Re_H = 2000$. The augmentation ratio peaks at 3.5 at $Re_H = 1200$–1500 for Case 2 and at 2.8 for Case 1 after which it decreases with the use of turbulent baseline values for normalization. As the flow reaches a fully turbulent state both geometries exhibit similar Nusselt number values (augmentation ratios between 2.3 and 2.5). This agrees with the experimental results reported by Moon et al. [7], where the Nusselt number augmentation exhibited a near constant value over $0.37 \leqslant H/D \leqslant 1.49$ in the fully turbulent regime.

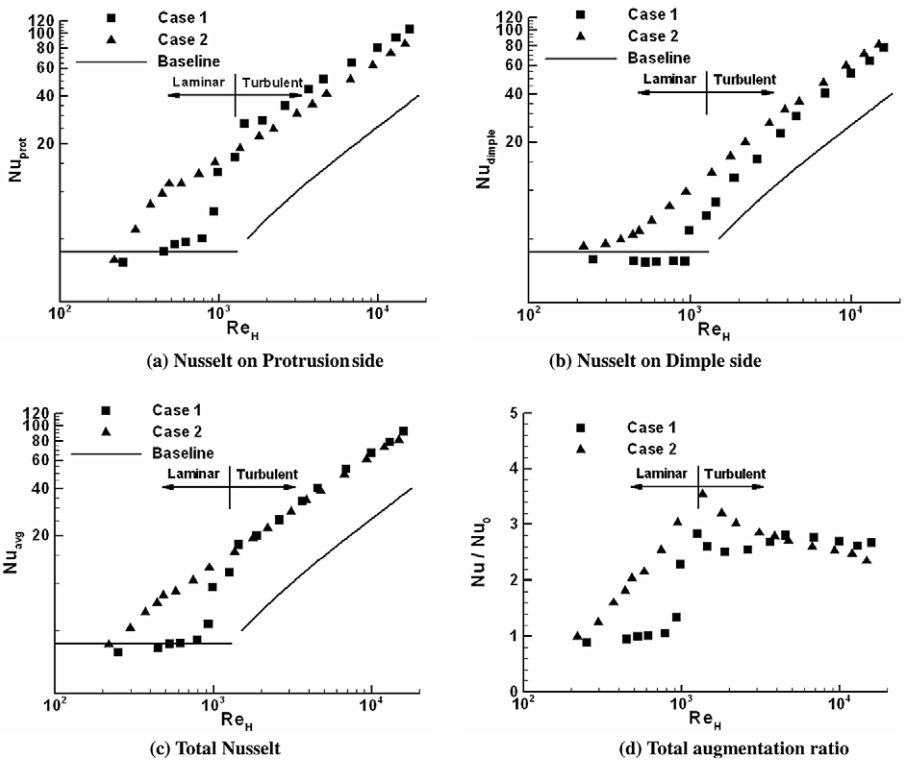

Fig. 12. Variation of Nusselt number with Re_H for Case 1 and Case 2.

A clear correlation exists between the time-mean volume averaged coherent vorticty plotted in Fig. 6, and the overall Nusselt number, Fig. 12. At low Reynolds numbers before transition, Case 1 exhibits a near constant magnitude of normalized vorticity which correlates with the near constant Nusselt number. In this range both vorticity and Nusselt number are higher in Case 2 than in Case 1. As the Reynolds number increases into the turbulent regime, the Nusselt numbers and coherent vorticity approach each other for the two cases but increase with Reynolds number. On the other hand, as mentioned earlier, normalized TKE not only approaches a near constant value in the turbulent regime but also remains higher in Case 2, unlike the trend in Nusselt number. This leads to the conclusion that trends in coherent vorticity magnitude is a better indicator of trends in heat transfer augmentation than turbulent kinetic energy.

8. Summary and conclusions

Direct and Large-Eddy Simulations are conducted in a channel with dimples and protrusions which is a realistic representation of finned compact heat exchangers. The Reynolds number range covers laminar, transitional and fully turbulent regimes. The same imprint pattern is investigated for two different fin pitches, Case 1 with twice the fin pitch of Case 2.

It is established that Case 1 provides little or no augmentation in the steady laminar flow regime up to a $Re_H = 900$ before the flow transitions to turbulence. Case 2 on the other hand, provides some augmentation in the laminar steady regime which lasts up to a $Re_H = 450$. As a consequence in the low Reynolds number regime $Re_H < 1000$, Case 2 exhibits superior augmentation properties. However, once the flow becomes turbulent in Case 1, there is no substantial difference between the two geometries after $Re_H = 3000$. Investigating the dynamics of heat transfer augmentation it was found that augmentation on the dimpled surface was chiefly brought about by vortex impingement in the reattachment region of the cavity. The ejection and redirection of these vortices and additional vortex shedding at the rim of the dimple was responsible for the high augmentation on the flat landing. On the protrusion side, flow impingement and acceleration between protrusions played an important role in augmenting heat transfer. Based on the variation of coherent vorticity with Reynolds number, it was concluded that the magnitude of volume-weighted time-averaged coherent vorticity correlated better with Nusselt number than did the volume averaged turbulent kinetic energy.

At low Reynolds number, Case 2 exhibited much higher friction losses than Case 1, but the difference decreased considerably in the fully turbulent regime. While friction drag dominated losses in Case 1 at low Reynolds numbers, both form and friction contributed equally in Case 2. As the Reynolds number increased to fully turbulent flow, form drag dominated in both cases contributing about 80% to the total losses. Unexpectedly, in Case 2, the dimple surface contributed about 70% of the total form drag.

In conclusion, the dimple/protrusion combination as a heat transfer enhancement surface produced mixed results.

While both geometries are viable and competitive with other augmentation surfaces such as ribs in the turbulent regime, Case 2 with the smaller fin pitch is more appropriate in the low Reynolds number regime $Re_H < 2000$, which makes up most of the operating range of typical compact heat exchangers.

Acknowledgements

This work is a result of support provided by the US Army RDECOM, Fort Belvoir, VA and Modine Manufacturing Co., Passenger Thermal Management, Racine, WI for air-side heat transfer enhancement in next generation compact heat exchangers. The support is gratefully acknowledged. The calculations were performed on Virginia Tech's Terascale computing facility, System-X.

References

[1] V.N. Afanasyev, Ya.P. Chudnovsky, A.I. Leontiev, P.S. Roganov, Turbulent flow friction and heat transfer characteristics for spherical cavities on a flat plate, Exp. Therm. Fluid Sci. 7 (1) (1993) 1–8.

[2] P.M. Ligrani, M.M. Oliveira, T. Blaskovich, Comparison of heat transfer augmentation techniques, AIAA J. 41 (3) (2003) 337–362.

[3] G.I. Mahmood, M.L. Hill, D.L. Nelson, P.M. Ligrani, Local heat transfer and flow structure on and above a dimpled surface in a channel, ASME Paper No. 2000-GT-230.

[4] P.M. Ligrani, J.L. Harrison, G.I. Mahmood, M.L. Hill, Flow structure due to dimple depressions on a channel surface, Phys. Fluids 13 (11) (2001) 3442–3451.

[5] P.M. Ligrani, N. Burgess, S. Won, Nusselt numbers and flow structure on and above a shallow dimpled surface within a channel including effects of inlet turbulence intensity level, J. Turbomach. 127 (2005) 321–330.

[6] M.K. Chyu, Y. Yu, H. Ding, J.P. Downs, F.O. Soechting, Concavity enhanced heat transfer in an internal cooling passage, ASME Paper No. 97-GT-437.

[7] H.K. Moon, T.O. O'Connell, B. Glezer, Channel height effect on heat transfer and friction in a dimpled passage, J. Eng. Gas Turb. Power 122 (2) (2000) 307–313.

[8] N.K. Burgess, P.M. Ligrani, Effects of dimple depth on Nusselt numbers and friction factors for internal cooling channel, ASME Paper No. GT2004-54232.

[9] S. Ekkad, H. Nasir, Dimple enhanced heat transfer in high aspect ratio channels, J. Enhanc. Heat Transfer 10 (4) (2003) 395–405.

[10] A.K. Borisov, S. Kobzar, B. Glezer, Comparison of thermo-hydraulic characteristics for two types of dimpled surfaces, ASME Paper No. GT2004-54204.

[11] T. Griffith, L. Al-Hadhrami, J.C. Han, Heat transfer in rotating rectangular cooling channels (AR = 4) with dimples, J. Turbomach. 125 (3) (2003) 555–563.

[12] P.M. Ligrani, G.I. Mahmood, J.L. Harrison, C.M. Clayton, D.L. Nelson, Flow structure and local Nusselt number variation in a channel with dimples and protrusions on opposite walls, Int. J. Heat Mass Transfer 44 (2001) 4413–4425.

[13] G.I. Mahmood, M.Z. Sabbagh, P.M. Ligrani, Heat transfer in a channel with dimples and protrusions on opposite walls, J. Thermophys. Heat Transfer 15 (3) (2001) 275–283.

[14] H.K. Moon, T. O'Connel, R. Sharma, Heat transfer enhancement using a convex-patterned surface, J. Turbomach. 125 (2) (2003) 274–280.

[15] Z. Wang, K.Z. Yeo, B.C. Khoo, Numerical simulation of laminar channel flow over dimpled surface, AIAA Paper No. AIAA 2003-3964.

[16] Y.L. Lin, T.I.-P. Shih, M.K. Chyu, Computations of flow and heat transfer in a channel with rows of hemispherical cavities, ASME Paper No. 99-GT-263.

[17] S.A. Isaev, A.I. Leont'ev, Numerical simulation of vortex enhancement of heat transfer under conditions of turbulent flow past a spherical dimple on the wall of a narrow channel, High Temp. 41 (5) (2003) 655–679.

[18] J. Park, P.R. Desam, P.M. Ligrani, Numerical predictions of flow structure above a dimpled surface in a channel, Numer. Heat Transfer A 45 (1) (2004) 1–20.

[19] S. Won, P.M. Ligrani, Numerical predictions of flow structure and local Nusselt number ratios along and above dimpled surfaces with different dimple depths in a channel, Numer. Heat Transfer A 46 (6) (2004) 549–570.

[20] J. Park, P.M. Ligrani, Numerical predictions of heat transfer and fluid flow characteristics for seven different dimpled surfaces in a channel, Numer. Heat Transfer A 47 (3) (2005) 209–232.

[21] W.V. Patrick, D.K. Tafti, Computations of flow structures and heat transfer in a dimpled channel at low to moderate reynolds number, ASME Paper No. HT-FED2004-56171.

[22] M. Elyyan, A. Rozati, D.K. Tafti, Study of flow structures and heat transfer in parallel fins with dimples and protrusions using large eddy simulation, ASME Paper No. FEDSM2006-98113.

[23] Z. Wang, K.S. Yeo, B.C. Khoo, DNS of low Reynolds number turbulent flows in dimpled channels, J. Turbul. 7 (37) (2006) 1–31.

[24] L. Zhang, D.K. Tafti, F. Najjar, S. Balachander, Computations of flow and heat transfer in parallel-plate fin heat exchangers on the CM-5: effects of flow unsteadiness and three-dimensionality, Int. J. Heat Mass Transfer 40 (66) (1997) 1325–1341.

[25] M. Germano, U. Piomelli, P. Moin, W.H. Cabot, A dynamic subgrid-scale eddy viscosity model, Phys. Fluids 3 (1991) 1760–1765.

[26] P. Moin, K. Squires, W. Cabot, S. Lee, A dynamic sub-grid-scale model for compressible turbulence and scalar transport, Phys. Fluids A 3 (11) (1991) 2746–2757.

[27] J. Cui, D.K. Tafti, Computations of flow and heat transfer in a three-dimensional multilouvered fin geometry, Int. J. Heat Mass Transfer 45 (2002) 5007–5023.

[28] E.A. Sewall, D.K. Tafti, A.B. Graham, K.A. Thole, Experimental validation of large eddy simulation of flow and heat transfer in a stationary ribbed duct, Int. J. Heat Fluid Flow 27 (2) (2006) 243–258.

[29] D.K. Tafti, GenIDLEST – A scalable parallel computational tool for simulating complex turbulent flows, Proc. ASME Fluids Engineering Division-*FED* 256 (2001) 346–357.

[30] F.P. Incropera, D.P. DeWitt, Fundamentals of Heat and Mass Transfer, fifth ed., Wiley, New York, 1996, pp. 463–493.

[31] W.V. Patrick, Computations of flow structure and heat transfer in a dimpled channel at low to moderate Reynolds number, Master's thesis, Virginia Tech, VA, 2005.

[32] D.K. Tafti, J. Cui, Fin tube junction effects on flow and heat transfer in flat tube multilouvered heat exchangers, Int. J. Heat Mass Transfer 45 (25) (2002) 5007–5023.

[33] M. Chong, A. Perry, B.J. Cantwell, A general classification of three-dimensional flow fields, Phys. Fluids A 2 (1990) 765–777.

[34] S.Y. Won, Q. Zhang, P.M. Ligrani, Comparisons of flow structure above dimpled surface with different dimple depths in a channel, Phys. Fluids 17 (4) (2005) 045105.